Puffing/micro-explosion in composite multi-component droplets

S.S. Sazhin[1*], E. Shchepakina[2], V.A. Sobolev[2], D.V. Antonov[3], P.A. Strizhak[3]

[1] *Advanced Engineering Centre, School of Architecture, Technology and Engineering, University of Brighton, Brighton, BN2 4GJ, UK*

[2] *Samara National Research University, 34, Moskovskoye Shosse, Samara 443086, Russia*

[3] *National Research Tomsk Polytechnic University, 30 Lenin Avenue, Tomsk, 634050, Russia*

October 25, 2021

Abstract

A new simple model for the puffing and micro-explosion of composite multi-component water/liquid fuel droplets is suggested. This model is based on the assumption that a spherical water sub-droplet is located in the centre of a spherical fuel droplet. The effects of droplet thermal swelling are considered; the Abramzon and Sirignano model is applied for the analysis of droplet heating and evaporation. It is assumed that puffing/micro-explosion starts when the temperature at the water/liquid fuel interface becomes equal to the water nucleation temperature. Assuming that the species diffusion coefficient is constant at each time step, the equation for species diffusion inside the droplet is solved analytically. Raoult's law at the surface of the droplet is used. The analytical solution to the equation for species diffusion is incorporated into the numerical code alongside the previously obtained analytical solution to the equation for heat transfer inside the droplet. Both solutions are used at each time step in the calculations. The model is used for the analysis of puffing/micro-explosion of kerosene/water droplets. The experimentally observed and predicted times to puffing/micro-explosion are shown to be reasonably close, decrease with increasing ambient gas temperatures and increase with increasing initial droplet radii. Taking into ac-

*Corresponding author: S.Sazhin@brighton.ac.uk

count the presence of multiple components in fuel leads to longer times to puffing/micro-explosion compared to the case when kerosene is approximated by cycloundecane (the dominant component in kerosene).

Keywords:
Composite droplets, puffing, micro-explosion, multi-component fuel, species diffusion equation

---

Nomenclature

c	specific heat capacity [J/(kg K)]
D	diffusion coefficient [m^2/s]
d_h	diameter of supporting cylinder [m]
$\mathcal{F}$	parameter defined by Expression (14) [-]
$\mathcal{G}$	parameter defined by Expression (15) [-]
h	convective heat transfer coefficient [W/(m^2 K)]
k	thermal conductivity [W/(m K)]
$\mathcal{K}$	parameter defined by the second expression in (16) [1/m]
L	heat of evaporation [J/(kg)]
ℓ	parameter defined by the first expression in (16) [m]
$\dot{m}_d$	droplet evaporation rate [kg/s]
p	pressure [Pa]
P	radiation source term [K/s]
q	parameter used in Expression (13) [m]
Q	parameter used in Expression (13) [m]
R	distance from the droplet centre [m]
S_C	contact area defined by Expression (23) [m^2]
t	time [s]
T	temperature [K]
v_n	eigenfunction [-]
X	molar fraction [-]
Y	mass fraction [-]

Greek symbols

α	parameter determined by Expression (10) [m/s]
ϵ	parameter determined by Expression (12) [-]
κ	thermal diffusivity [m^2/s]
λ_n	eigenvalue [-]

ρ	density [kg/m^3]
τ_p	time to puffing/micro-explosion [s]

Subscripts

av	average
c	centre
d	droplet
(e)	evaporation
eff	effective
f	fuel
g	gas
i	fuel components
l	liquid
s	surface
sup	support
v	vapour
w	water or water/fuel interface
0	initial condition
∞	ambient condition

1. Introduction

The importance of puffing (the partial ejection of the water outside fuel droplets) and micro-explosion (the total break-up of droplets) in water/fuel composite droplets to the improvement of internal combustion engine performance has been commonly recognised (e.g. [1]). This stimulated numerous experimental and theoretical studies of the phenomena some of which are summarised in [2, 3].

The most advanced models of these processes suggested so far are based on high-fidelity direct numerical simulations (DNS) from first principles [4, 5, 6, 7]. These models were supplemented by several simplified models of the phenomena [8, 2, 9, 10, 11]. Without discussing the details of these models, we mention that in all of them fuel was assumed to be mono-component; the limitations of this approximation have been widely discussed [12].

The main objective of the new paper is to suggest a new simple model of puffing/micro-explosion in which the effects of multiple components in liquid

fuel are considered. The main ideas of the model described in [2] will be incorporated in the new model.

Key equations/approximations used in the new model are summarised in Section 2. The new numerical algorithm, developed based on this model, is introduced in Section 3. Section 4 focuses on the summary of experimental observations of puffing/micro-explosion in kerosene/water droplets, as examples of multi-component composite droplets. The application of the newly developed model to the latter droplets is demonstrated in Section 5. The most important results are presented in Section 6.

2. Basic equations and approximations

The new model is based on the same assumptions and equations as the model described in [2], which are supplemented by new developments for modelling the processes in multi-component fuels. A spherical water sub-droplet of radius R_w is located in the centre of a spherical liquid fuel droplet of radius R_d. The spatial and temporal evolution of the temperature inside the composite droplet is described by the following transient heat transfer equation:

$$\frac{\partial T}{\partial t} = \kappa \left(\frac{\partial^2 T}{\partial R^2} + \frac{2}{R} \frac{\partial T}{\partial R} \right) + P(R,t), \tag{1}$$

where

$$\kappa = \begin{cases} \kappa_w = k_w/(c_w \rho_w) & \text{for} \quad R \le R_w \\ \kappa_f = k_f/(c_f \rho_f) & \text{for} \quad R_w < R \le R_d, \end{cases} \tag{2}$$

$k_{w(f)}$, $c_{w(f)}$, and $\rho_{w(f)}$ are the thermal conductivity, specific heat capacity, and density of water (liquid fuel), respectively; R the distance from the centre of the droplet, t time. $P(R,t)$ describes the droplet internal heating (e.g. heating by thermal radiation penetrating inside the droplet).

Equation (1) was solved analytically with the initial and boundary conditions:

$$T(t=0) = \begin{cases} T_{w0}(R) & \text{when} \quad R \le R_w \\ T_{f0}(R) & \text{when} \quad R_w < R \le R_d, \end{cases} \tag{3}$$

$$T|_{R=R_w^-} = T|_{R=R_w^+}, \qquad k_w \left. \frac{\partial T}{\partial R} \right|_{R=R_w^-} = k_f \left. \frac{\partial T}{\partial R} \right|_{R=R_w^+}, \tag{4}$$

$$h\left(T_{\text{eff}} - T(R_d)\right) = k_f \left.\frac{\partial T}{\partial R}\right|_{R=R_d-0}, \tag{5}$$

h is the convective heat transfer coefficient,

$$T_{\text{eff}} = T_g + \frac{\rho_f L \dot{R}_{d(e)}}{h}.$$

It is assumed that $T_{w0}(R_w) = T_{f0}(R_w)$. $\left.\dot{R}_{d(e)} \equiv dR_d/dt\right|_{\rho_f=\text{const}}$ takes into account the change in R_d due to evaporation. The Abramzon and Sirignano model [14] is used to estimate the evaporation rate and h.

The changes in droplet radii due to thermal swelling during individual time steps are estimated as [2]:

$$\Delta R_{d(s)} \equiv R_{d1} - R_{d0} = R_{d0}\left\{\left[\left(1 - \frac{R_{w0}^3}{R_{d0}^3}\right)\frac{\rho_{f0}}{\rho_{f1}} + \frac{R_{w0}^3}{R_{d0}^3}\frac{\rho_{w0}}{\rho_{w1}}\right]^{1/3} - 1\right\}, \tag{6}$$

where subscripts $_0$ and $_1$ refer to the beginning and end of the time step, respectively.

An explicit solution to Equation (1) subject to Conditions (2)-(4) is given in [2]. This solution was incorporated into the numerical code and used at each step in the calculation. In contrast to the model described in [2], the model used in our analysis takes into account the multi-component nature of fuel in the shell surrounding the water sub-droplet.

The following equations for mass fractions $Y_{li} \equiv Y_{li}(t, R)$ inside the liquid multi-component liquid fuel shell surrounding water sub-droplets were used:

$$\frac{\partial Y_{li}}{\partial t} = D_l\left(\frac{\partial^2 Y_{li}}{\partial R^2} + \frac{2}{R}\frac{\partial Y_{li}}{\partial R}\right), \tag{7}$$

where $i \geq 1$, D_l is the liquid fuel mass diffusivity; this is assumed to be constant for all species. Equation (7) is solved using the conditions at the outer and inner boundaries of the shell:

$$\alpha(\epsilon_i - Y_{lis}) = -D_l \left.\frac{\partial Y_{li}}{\partial R}\right|_{R=R_d-0}, \tag{8}$$

$$\left.\frac{\partial Y_{li}}{\partial R}\right|_{R=R_w+0} = 0, \tag{9}$$

where $Y_{lis} = Y_{lis}(t)$ are mass fractions of components i at the droplet's surface,

$$\alpha = |\dot{m}_d| \left[4\pi\rho_l R_d^2\right]^{-1}, \tag{10}$$

$\dot{m}_d$ is the rate of droplet evaporation, and the initial condition:

$$Y_{li}(R,t)|_{t=0} \equiv Y_{li0}(R). \tag{11}$$

Equation (8) is a well known boundary condition for evaporating multicomponent droplets [13]. Equation (9) is a statement that no fuel species penetrate from the fuel shell into water.

We assume that [13]:

$$\epsilon_i = \frac{Y_{vis}}{\sum_i Y_{vis}}, \tag{12}$$

where subscript $_v$ shows the vapour phase.

The analytical solution to Equation (7) subject to Conditions (8), (9), and (11) was obtained as (see Appendix 1 for the details):

$$Y_{li} = \epsilon_i + \frac{1}{R}\left\{\exp\left[D_l\left(\frac{\lambda_0}{R_d}\right)^2 t\right]\right\}\left[q_{i0} - \epsilon_i Q_0\right] v_0$$

$$+\frac{1}{R}\sum_{n=1}^{\infty}\left\{\exp\left[-D_l\left(\frac{\lambda_n}{R_d}\right)^2 t\right]\right\}\left[q_{in} - \epsilon_i Q_n\right] v_n, \tag{13}$$

where eigenvalues λ_0 and λ_n $(n \geq 1)$ are positive solutions to the following equations:

$$\mathcal{F} \equiv \left(\ell\mathcal{K} - \frac{R_w\left(\frac{\lambda_0}{R_d}\ell\right)^2}{\ell}\right)\tanh\left(\frac{\lambda_0}{R_d}\ell\right) = \left(\frac{\lambda_0}{R_d}\ell\right)(1 - R_w\mathcal{K}), \tag{14}$$

$$\mathcal{G} \equiv \left(\ell\mathcal{K} + \frac{R_w\left(\frac{\lambda_n}{R_d}\ell\right)^2}{\ell}\right)\tan\left(\frac{\lambda_n}{R_d}\ell\right) = \left(\frac{\lambda_n}{R_d}\ell\right)(1 - R_w\mathcal{K}), \quad (n \geq 1) \tag{15}$$

$$\ell = R_d - R_w, \qquad \mathcal{K} = \frac{1}{R_d}\left[1 + \frac{\alpha R_d}{D_l}\right]. \tag{16}$$

$$v_0 = \sinh\left(\frac{\lambda_0}{R_d}(R - R_w)\right) + \frac{\lambda_0 R_w}{R_d}\cosh\left(\frac{\lambda_0}{R_d}(R - R_w)\right), \tag{17}$$

$$v_n = \sin\left(\frac{\lambda_n}{R_d}(R - R_w)\right) + \frac{\lambda_n R_w}{R_d}\cos\left(\frac{\lambda_n}{R_d}(R - R_w)\right), \quad (n \geq 1) \tag{18}$$

$$q_{in} = \frac{1}{||v_n||^2}\int_0^\ell (\mathcal{R} + R_w) Y_{li0}(\mathcal{R} + R_w) v_n(\mathcal{R}) \mathrm{d}\mathcal{R}, \quad (n \geq 0) \tag{19}$$

$$Q_n = \frac{1}{||v_n||^2}\int_0^\ell (\mathcal{R} + R_w) v_n(\mathcal{R}) \mathrm{d}\mathcal{R}, \quad (n \geq 0) \tag{20}$$

$\mathcal{R} = R - R_w$, ϵ_i are the initial values of this parameter at each time step, expressions for norms $||v_n||^2 \quad (n \geq 0)$ are given by (72) and (73).

Solution (13) was obtained using the assumption that the processes are spherically symmetric; the effect of droplet velocity was not considered. In the case of homogeneous droplets, the latter effect could be considered using the Effective Diffusivity model [13]. Unfortunately, in the case of composite droplets this model cannot be combined with the model used in the paper (the assumption about the central location of the water sub-droplet is not consistent with the assumption of the formation of the Hill vortex used in the ED model).

In our analysis Solution (13) is applied to both stationary and moving droplets. For the corresponding analytical solution to Equation (1), a non-self-consistent model suggested in [3] is used to describe the heating of moving composite droplets. In this model, the rate of heating of droplets by the gas takes into account the droplet's movement but the processes inside the droplet are assumed not to be affected by this movement.

The partial pressure of vapour component i at the droplet surface is found from Raoult's law:

$$p_{vsi} = X_{lsi} p^*_{vi}, \tag{21}$$

where X_{lsi} are the molar fractions of the ith liquid species in the immediate vicinity of the droplet surface, p^*_{vi} are the partial vapour pressures of the ith species for $X_{lsi} = 1$.

The contribution of a droplet's support on its heating is considered following the model described in [15]. In this model the effect of the support is described via the introduction of the following approximation of $P(R)$ in Equation (1):

$$P(R) = \frac{3k_f(T_{\mathrm{sup}} - T_c)}{4\pi c_f \rho_f R_d^4} S_C, \tag{22}$$

where T_{sup} and T_c are the temperature of the support and that at the droplet centre, respectively, S_C is the the area of the droplet that is in contact with

the cylindrical support which is estimated as:

$$S_C = \pi d_{\rm h} R_d, \tag{23}$$

$d_{\rm h}$ is the diameter of the supporting cylinder.

The contribution of vapour to the transport/thermodynamic properties of ambient gas is ignored. The effect of the relative diffusion of vapour components is not considered. For in-depth discussion of the latter effect see [16, 17]. The Abramzon and Sirignano model was applied to the analysis of the droplet heating and evaporation [13].

Puffing/micro-explosion is assumed to start when the temperature at the interface between water and liquid fuel (T_w) reaches the water nucleation temperature (T_N). The latter temperature is found from the boiling temperature of water and the rate of change of the temperature at the water-fuel interface with time ($\dot{T}$), applying one of the correlations suggested in [2] for various ranges of $\dot{T}$. The values of $\dot{T}$ at this interface were obtained at each time step using the analytical solution to Equation (1) at each time step. The time to puffing/micro-explosion was found as a point of intersection of the curves $T_w(t)$ and $T_N(t)$ (see [2] for the details). As in [2], the effect of bubble growth on time to puffing/micro-explosion was not considered.

3. Numerical code

Both the analytical solution to the equation for species diffusion derived earlier and the analytical solution to the equation for heat transfer derived in [2] were implemented into the numerical code and used at each time step of the calculations (see [13, 2] for the details).

Calculations were performed using Matlab R2020a. One hundred terms were used in series (13) and 200 terms were used in the corresponding series in the analytical solution for temperature (see Expression (11) in [2]); no difference in the results was noticed when these numbers of terms increased further. Time steps 50 μs and 0.1 s were used for the smallest and largest droplets, respectively; 10,000 cells along the droplet radius were used to calculate integrals for the parameters in (13) and Expression (11) in [2].

The roots of Equations (14) and (15) and the corresponding equation for temperature (Equation (12) in [2]) were obtained using the bisection method with absolute accuracy of 10^{-15}. The graphical illustrations of solutions of (14) and (15) are shown in Appendix 3.

The results of calculations using the new code were verified by comparing its predictions with those inferred from ANSYS Fluent, in which the analytical solution described in Section 2 in the limits $R_w = 0$ was implemented via User Defined Functions (UDF) [18]. The details are shown in Appendix 4.

4. Kerosene droplets: experimental set-up

The model and numerical code described in Sections 1 and 2 were applied to the investigation of puffing/micro-explosion in composite kerosene (JetA-1)/distilled water (Russian standard 6709-72) droplets which can be considered as a typical example of multi-component composite droplets. The volume fractions of kerosene and water used in the experiments were 90% and 10%, respectively. This choice of composite droplet parameters was based on the previous investigation [19] where it was shown that for these parameters puffing and micro-explosion were consistently observed for a wide range of ambient temperatures (450-850 K) and initial droplet radii (0.5-1.0 mm). The model is obviously applicable to any other multi-component fuel.

The methodology used for the generation of composite droplets was similar to the one described in [20]. Two electronic Finnpipette Novus dispensers, designed to take in liquid volumes in the ranges 5 to 50 μl (with steps of 0.1 μl) and 0.5 to 12.5 μl (with steps of 0.01 μl), were used. These dispensers were equipped with special replaceable tips for liquid intake. First, a water droplet was generated and mounted on a holder. Then a fuel droplet was generated which spread over the surface of the water droplet forming a film of thickness 0.05 to 0.5 mm [21]. The ratio of the volumes of water and fuel (1:9) was maintained with errors less than 3%. Planar Laser Induced Fluorescence (PLIF) was used to determine the thickness of kerosene films. A Rhodamine B solution of 10000 μg/l was added to water; it was illuminated by a laser sheet as in [21].

To investigate time to puffing/micro-explosion an experimental set-up similar to the one described in [22] was used. The processes of composite droplet evaporation and disintegration were recorded using a high speed Phantom Miro M310 video camera (Vision Research, USA, with the following specifications: maximal speed 3260 frames per second (fps) at full resolution 1280x800 pixels; 12 bit depth; 1 μs minimum exposure; pixel size 20 μm; 12 Gb memory; image-based auto-trigger). The images were taken at frequencies 1000 to 10000 fps with resolutions of 640x480 pixels. The video frames

were processed using Phantom Camera Control software and the start of droplet desintegration was identified. Systematic errors of determination of times to puffing/micro-explosion did not exceed ± 1 μs. The initial droplet diameters were measured at the time instant when droplets were introduced into the camera. These diameters were inferred by averaging droplet sizes in two perpendicular directions.

Each measurement was performed at least 5-10 times with identical conditions, including ambient temperatures, initial droplet sizes and volume fractions of the components.

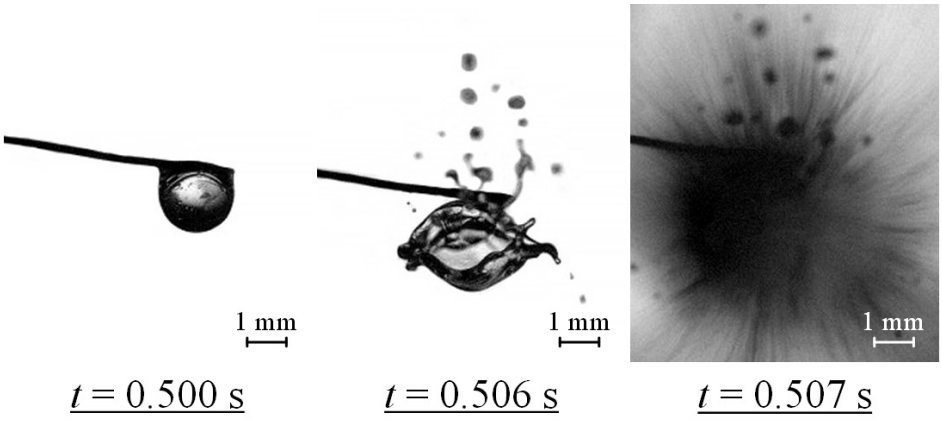

Figure 1: Typical images of puffing/micro-explosion observed in the experiments. A kerosene/water composite droplet (initial radius $R_{d0} = 0.92$ mm and volume fraction of water $V_{w0} = 10\%$) was placed in a muffle furnace at atmospheric pressure and ambient temperature $T_g = 723$ K.

Typical video frames showing the evaporation and disintegration of composite kerosene/water droplets are shown in Figure 1.

5. Modelling and experimental results

The kerosene composition presented in Table 1 of [23] was used for our analysis. The transport/thermodynamic properties of kerosene components shown in this table are presented in the Supplementary Material of [23] (see also the Supplementary Material of [24]). Some corrections and more accurate approximations of these properties are presented in the Supplementary Material of this paper.

The diffusion coefficient for liquid species is inferred from the Wilke-Chang formula with the molar mass equal to the average molar mass of all species [25]. It is assumed that kerosene vapour can be approximated by the dominant component (cycloundecane), and the following formula for the vapour diffusion coefficient (in m^2/s) was used for atmospheric pressure [23]:

$$D_v = \left[-0.04025 + 2.4907 \times 10^{-4} \times T + 3.1411 \times 10^{-7} \times T^2\right] \times 10^{-4}, \quad (24)$$

where T is the reference temperature of gas in K.

Liquid thermodynamic/transport properties were estimated at the droplet average temperatures at specific time steps. The latent heat of evaporation and saturated vapour pressure were estimated at the surface temperatures of the droplets.

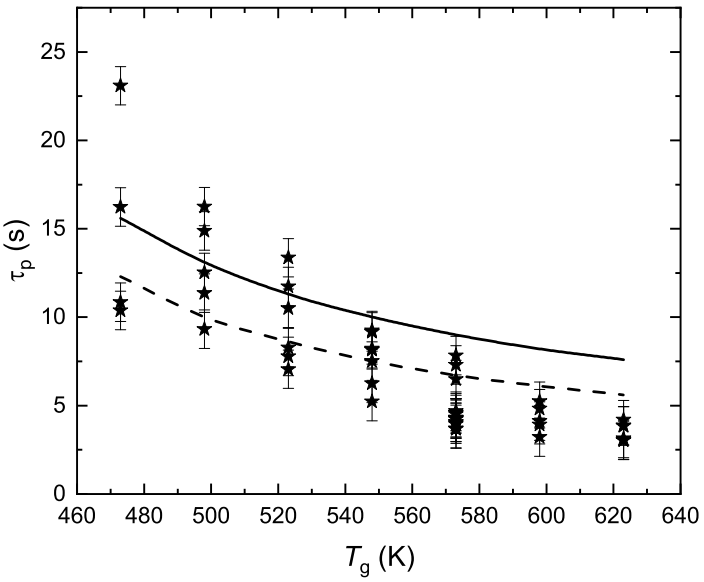

Figure 2: Times to puffing/micro-explosion of water/kerosene droplets (τ_p) versus gas temperatures T_g, observed experimentally (stars) and predicted by the model assuming that puffing/micro-explosion starts when the temperature at the water/kerosene interface becomes equal to the water nucleation temperature ($T_w = T_N$) (curves). The solid curve shows the case when the contributions of all kerosene components were considered; the dashed curve shows the case when kerosene was approximated by cycloundecane.

The observed times to puffing/micro-explosion τ_p versus gas temperatures are shown in Figure 2. Our analysis was focused on kerosene/water composite droplets with initial temperature 300 K, radii 0.85 mm and volumetric

water content 10% ($R_w = 0.395$ mm). The experiments were performed at atmospheric pressure. In the same figure, the values of τ_p predicted by the numerical code are shown. It was assumed that puffing and micro-explosion start when the temperature at the water/kerosene interface (T_w) becomes equal to the water nucleation temperature (T_N). We followed the methodology developed in [2] to find this time.

Two cases were investigated. Firstly, the contributions of all kerosene components were considered using the model described in Section 2. Secondly, kerosene was approximated by cycloundecane and a much simpler model described in [2] was used. As can be seen from Figure 2, in both cases the predictions of the numerical code show the same trend of the reduction of τ_p with an increase in ambient gas temperatures. The predictions of the code using both approximations of kerosene are reasonably close to experimental data. The code considering the contributions of all kerosene components predicts longer τ_p than that in which kerosene was approximated by cycloundecane.

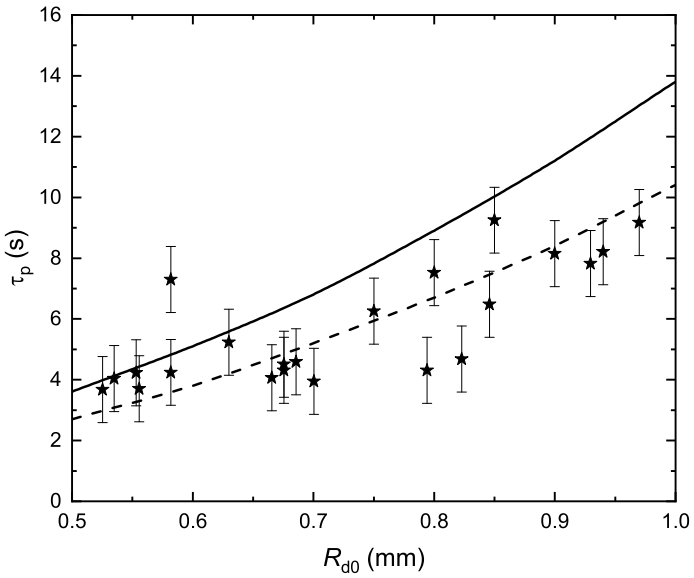

Figure 3: The same as Figure 2 but for times to puffing or micro-explosion versus the initial droplet radii.

The experimentally observed times to puffing/micro-explosion τ_p versus initial droplet radii are shown in Figure 3. Our analysis focused on

kerosene/water composite droplets with volumetric water content 10% placed in gas at temperature 548 K. Also as in Figure 2, in all cases the initial droplet temperatures were 300 K. As in Figure 2, we considered the cases when the contributions of all kerosene components were taken into account and when kerosene was approximated by cycloundecane.

As can be seen from Figure 3, in both cases the prediction of the numerical code shows the same increase in τ_p with an increase in droplet initial radii as observed experimentally. As in the case of Figure 2, the predictions of the code using both approximations of kerosene are reasonably close. The code considering the contributions of all kerosene components predicts longer τ_p than in the case when kerosene was approximated by cycloundecane. Note that our model tends to predict longer times to puffing/micro-explosion compared with those observed experimentally as it uses the assumption that the water sub-droplet is located in the centre of the kerosene droplet. See [2] for further discussion of this matter.

6. Conclusions

A new simple model of puffing/micro-explosion of multi-component composite water/liquid fuel droplets is suggested. This model uses the same assumptions as the model described in [2] except that the effects of the multi-component nature of the fuel are considered. Following [2], it is assumed that a water sub-droplet is located in the centre of a spherical fuel droplet. The analysis of the heating of a composite droplet is based on the heat conduction equation. The Robin boundary condition at the droplet surface and continuity conditions at the water/liquid fuel interface are used. The analytical solution to this equation is incorporated into the numerical code and used for the analysis of puffing/micro-explosion in droplets at each time step. The effects of droplet thermal swelling are considered. The Abramzon and Sirignano model is applied to the analysis of droplet heating and evaporation. It is assumed that puffing/micro-explosion are triggered when the temperature at the water/fuel interface becomes equal to the water nucleation temperature.

In contrast to [2], the multi-component nature of the fuel is considered. Making an assumption that the liquid diffusion coefficient is constant for all species at each time step, the species diffusion equation inside the droplets is solved analytically. In this solution it is taken into account that fuel species do not penetrate into water. Raoult's law is used at the surface of the droplet. The relative diffusion of individual species in the gas phase is not taken into

account. The analytical solution to the species diffusion equation in the liquid phase is incorporated into the numerical code alongside the previously obtained analytical solution for the distribution of temperature inside the droplets. Both solutions are used at each time step of the calculation.

The model is used for the analysis of puffing/micro-explosion of kerosene/water composite droplets. The results of experimental studies of these droplets are presented. Their volumetric water content was taken equal to 10%. Droplets with initial radii in the range 0.5 to 1 mm were investigated. The ambient gas temperature in the experiments was in the range 450 to 850 K.

It is shown that both experimentally observed and predicted times to puffing/micro-explosion are reasonably close, decreasing with increasing ambient gas temperatures and increasing with increasing initial droplet radii. Considering the presence of multiple components in liquid fuel leads to an increase in the time to puffing/micro-explosion compared to the case when kerosene is approximated by a single component (cycloundecane).

Acknowledgement

The authors are grateful for the financial support received from the Russian Science Foundation (Grant 21-19-00876), which supported S. S. Sazhin (who contributed to the development of the physical and mathematical models, analysis of the results and preparation of the text of the paper), E. Shchepakina and V.A. Sobolev (who contributed to the development of the mathematical model), Scholarship from the President of the Russian Federation (Grant SP-447.2021.1) which supported D. Antonov (who performed the experiments and applied the model to their analysis), and the National Research Tomsk Polytechnic University (project VIU-ISHFVP-60/2019) which supported P.A. Strizhak (who contributed to the preparation of the experiments and the analysis of the results).

Appendix 1

Solution of Equation (7)

In this Appendix, the details of the solution of Equation (7) ($Y_{li}(t,R)$) for $t \geq 0$ and $R_w \leq R \leq R_d$ are presented.

Let us rewrite Condition (8) as:

$$\left(\frac{\partial Y_{li}}{\partial R} - \frac{\alpha}{D_l} Y_{li}\right)\Bigg|_{R=R_d} = -\alpha \epsilon_i(t) D_l^{-1}. \tag{25}$$

We look for a solution to Equation (7) as:

$$Y_{li}(t,R) = y(t,R) + \epsilon(t), \tag{26}$$

where subscript i at y and ϵ is hereafter omitted.

Having substituted (26) into Equation (7) and Conditions (25), (9) and (11) we can rewrite this equation and the corresponding boundary and initial conditions as:

$$\frac{\partial y}{\partial t} = D_l \left(\frac{\partial^2 y}{\partial R^2} + \frac{2}{R}\frac{\partial y}{\partial R} \right) - \frac{\mathrm{d}\epsilon(t)}{\mathrm{d}t}, \tag{27}$$

$$\left(\frac{\partial y}{\partial R} - \frac{\alpha}{D_l} y \right)\Bigg|_{R=R_d-0} = 0, \tag{28}$$

$$\frac{\partial y}{\partial R}\Bigg|_{R=R_w+0} = 0, \tag{29}$$

$$y(t=0) = Y_{li0}(R) - \epsilon(0) \equiv Y_{li0}(R) - \epsilon_0. \tag{30}$$

Using new variable

$$\mathcal{R} = R - R_w \tag{31}$$

and ignoring the contribution of the term $\frac{\mathrm{d}\epsilon(t)}{\mathrm{d}t}$ in Equation (27)[1], we can rewrite (27)-(30) as:

$$\frac{\partial y}{\partial t} = D_l \left(\frac{\partial^2 y}{\partial \mathcal{R}^2} + \frac{2}{\mathcal{R} + R_w}\frac{\partial y}{\partial \mathcal{R}} \right), \tag{32}$$

$$\left(\frac{\partial y}{\partial \mathcal{R}} - \frac{\alpha}{D_l} y \right)\Bigg|_{\mathcal{R}=R_d-R_w} = 0, \tag{33}$$

$$\frac{\partial y}{\partial \mathcal{R}}\Bigg|_{\mathcal{R}=0} = 0, \tag{34}$$

$$y|_{t=0} = Y_{li0}(\mathcal{R} + R_w) - \epsilon(0) \equiv Y_{li0}(\mathcal{R} + R_w) - \epsilon_0. \tag{35}$$

[1]This assumption is consistent with other assumptions made in our analysis, remembering that the final solution will be used during short time steps in the numerical codes, including the assumption that $R_d = \text{const}$ during individual time steps. The validity of this assumption was confirmed using the numerical analysis of the evaporation in multi-component droplets without water sub-droplets ($R_w = 0$) taking and not taking into account this term in the analytical solution [18].

Using new variable

$$u(t,\mathcal{R}) = y(t,\mathcal{R})(\mathcal{R}+R_w)$$

allows us to rewrite (32)-(35) as:

$$\frac{\partial u}{\partial t} = D_l \frac{\partial^2 u}{\partial \mathcal{R}^2}, \tag{36}$$

$$\left(\frac{\partial u}{\partial \mathcal{R}} - \left(\frac{1}{R_d}+\frac{\alpha}{D}\right)u\right)\Bigg|_{\mathcal{R}=R_d-R_w} = 0, \tag{37}$$

$$\left(R_w\frac{\partial u}{\partial \mathcal{R}} - u\right)\Bigg|_{\mathcal{R}=0} = 0, \tag{38}$$

$$u(\mathcal{R},0) = (\mathcal{R}+R_w)\left(Y_{li0}(\mathcal{R}+R_w) - \epsilon_0\right). \tag{39}$$

We look for a solution to Equation (36) as:

$$u = \sum_{n=0}^{\infty} \Theta_n(t) v_n(\mathcal{R}), \tag{40}$$

where $v_n(\mathcal{R})$ is the full set of non-trivial solutions to the equation:

$$\frac{\partial^2 v}{\partial \mathcal{R}^2} + pv = 0, \tag{41}$$

with the boundary conditions:

$$\left(\frac{\partial v}{\partial \mathcal{R}} - \left(\frac{1}{R_d}+\frac{\alpha}{D}\right)v\right)\Bigg|_{\mathcal{R}=R_d-R_w} = 0, \tag{42}$$

$$\left(R_w\frac{\partial v}{\partial \mathcal{R}} - v\right)\Bigg|_{\mathcal{R}=0} = 0. \tag{43}$$

Note that p in this approach is dimensional and has units of $1/\mathrm{m}^2$.

Equation (41) with boundary conditions (42) and (43) is the Sturm-Liouville problem. We consider separately the cases when $p < 0$, $p = 0$, and $p > 0$.

Sturm-Liouville problem for $p < 0$

Assuming that $p = -(\lambda/R_d)^2$, the general solution to Equation (41) can be presented as

$$v = A \sinh\left(\frac{\lambda \mathcal{R}}{R_d}\right) + B \cosh\left(\frac{\lambda \mathcal{R}}{R_d}\right). \tag{44}$$

Note that λ is dimensionless. Having substituted (44) into (42) and (43) we obtain:

$$A\left[\frac{\lambda}{R_d}\cosh\left(\frac{\lambda\ell}{R_d}\right) - \mathcal{K}\sinh\left(\frac{\lambda\ell}{R_d}\right)\right] + B\left[\frac{\lambda}{R_d}\sinh\left(\frac{\lambda\ell}{R_d}\right) - \mathcal{K}\cosh\left(\frac{\lambda\ell}{R_d}\right)\right] = 0, \tag{45}$$

$$A\frac{\lambda R_w}{R_d} - B = 0, \tag{46}$$

where

$$\ell = R_d - R_w, \qquad \mathcal{K} = \frac{1}{R_d}\left[1 + \frac{\alpha R_d}{D_l}\right]. \tag{47}$$

System (45) and (46) has a non-trivial solution if and only if its determinant is equal to zero, which implies that:

$$\Delta(\lambda) = \left(\frac{R_w\lambda^2}{R_d^2} - \mathcal{K}\right)\sinh\left(\frac{\lambda\ell}{R_d}\right) + \frac{\lambda}{R_d}(1 - R_w\mathcal{K})\cosh\left(\frac{\lambda\ell}{R_d}\right) = 0. \tag{48}$$

Equation (48) can be simplified to

$$\tanh\left(\frac{\lambda\ell}{R_d}\right) = \frac{\lambda(1 - R_w\mathcal{K})}{R_d\left(\mathcal{K} - \frac{R_w\lambda^2}{R_d^2}\right)}. \tag{49}$$

Equation (49) can be further rearranged to

$$\mathcal{F}(\tilde{\lambda}) \equiv \left(\ell\mathcal{K} - \frac{R_w\tilde{\lambda}^2}{\ell}\right)\tanh\tilde{\lambda} = \tilde{\lambda}(1 - R_w\mathcal{K}). \tag{50}$$

where $\tilde{\lambda} = \lambda\ell/R_d$. The graphical solution to Equation (50) is the intersection of $\mathcal{F}(\tilde{\lambda})$ with the straight line described by the right hand side of (50). Using the same input parameters as in Section 5 the details of this solution are shown in Appendix 3. As follows from the analysis presented

in this Appendix, Equation (50) has only one solution for these values of parameters.

In the limit $R_w = 0$ Equation (50) reduces to Equation (H.15) of [13]. Solution $\tilde{\lambda} > 0$ to Equation (50) will be referred to as $\tilde{\lambda}_0$ which corresponds to λ_0.

Assuming that $A = 1$ we have from Equation (46) that $B = \lambda R_w/R_d = \tilde{\lambda} R_w/\ell$. For $\lambda = \lambda_0$, Solution (44) can be presented as:

$$v_0 = \sinh\left(\frac{\lambda_0 \mathcal{R}}{R_d}\right) + \frac{\lambda_0 R_w}{R_d}\cosh\left(\frac{\lambda_0 \mathcal{R}}{R_d}\right), \tag{51}$$

where $\lambda_0 = \tilde{\lambda_0} R_d/\ell$ is obtained from (50). Note that our assumption $A = 1$ does not affect the generality of the solution since the normalisation of u will be obtained when calculating Θ.

Formula (51) can be presented in an alternative form:

$$v_0 = A_{Y0}\sinh\left(\frac{\lambda_0 \mathcal{R}}{R_d} + \eta_{Y0}\right). \tag{52}$$

To obtain explicit expressions for coefficients A_Y and η_Y we rewrite (52) as

$$v_0 = A_{Y0}\sinh\left(\frac{\lambda_0 \mathcal{R}}{R_d}\right)\cosh\eta_{Y0} + A_{Y0}\cosh\left(\frac{\lambda_0 \mathcal{R}}{R_d}\right)\sinh\eta_{Y0}, \tag{53}$$

Comparing (51) and (53) we obtain:

$$\cosh\eta_{Y0} = \frac{1}{A_{Y0}}; \quad \sinh\eta_{Y0} = \frac{\lambda_0 R_w}{R_d A_{Y0}}; \quad \tanh\eta_{Y0} = \frac{\lambda_0 R_w}{R_d}, \tag{54}$$

Remembering that

$$\cosh^2\eta_{Y0} - \sinh^2\eta_{Y0} = \left(\frac{1}{A_{Y0}}\right)^2 - \left(\frac{\lambda_0 R_w}{R_d A_{Y0}}\right)^2 = 1$$

we obtain:

$$A_{Y0} = \sqrt{1 - \left(\frac{\lambda_0 R_w}{R_d}\right)^2}. \tag{55}$$

Sturm-Liouville problem for $p = 0$

For $p = 0$ the general solution to Equation (41) can be presented as

$$v = A\mathcal{R} + B. \tag{56}$$

Having substituted (56) into (42) and (43) we obtain:

$$A(1 - \mathcal{K}\ell) - B\mathcal{K} = 0, \quad AR_w - B = 0. \tag{57}$$

The determinant of this system is equal to zero if and only if

$$\mathcal{K}(\ell + R_w) = R_d\mathcal{K} = 1, \tag{58}$$

which is not possible since $\mathcal{K} > 1/R_d$.

Sturm-Liouville problem for $p > 0$

Assuming that $p = (\lambda/R_d)^2$, the general solution to Equation (41) can be presented as

$$v = A \sin\left(\frac{\lambda\mathcal{R}}{R_d}\right) + B \cos\left(\frac{\lambda\mathcal{R}}{R_d}\right). \tag{59}$$

Having substituted (59) into (42) and (43) we obtain:

$$A\left[\frac{\lambda}{R_d}\cos\left(\frac{\lambda\ell}{R_d}\right) - \mathcal{K}\sin\left(\frac{\lambda\ell}{R_d}\right)\right] + B\left[-\frac{\lambda}{R_d}\sin\left(\frac{\lambda\ell}{R_d}\right) - \mathcal{K}\cos\left(\frac{\lambda\ell}{R_d}\right)\right] = 0, \tag{60}$$

$$A\frac{\lambda R_w}{R_d} - B = 0. \tag{61}$$

System (60) and (61) has a non-trivial solution if and only if its determinant is equal to zero, which implies that:

$$\Delta(\lambda) = -\left(\frac{R_w\lambda^2}{R_d^2} + \mathcal{K}\right)\sin\left(\frac{\lambda\ell}{R_d}\right) + \frac{\lambda}{R_d}(1 - R_w\mathcal{K})\cos\left(\frac{\lambda\ell}{R_d}\right) = 0. \tag{62}$$

Equation (62) can be simplified to

$$\tan\left(\frac{\lambda\ell}{R_d}\right) = \frac{\lambda(1 - R_w\mathcal{K})}{R_d\left(\mathcal{K} + \frac{R_w\lambda^2}{R_d^2}\right)}. \tag{63}$$

Equation (63) can be further rearranged to

$$\mathcal{G}(\tilde{\lambda}) \equiv \left(\ell\mathcal{K} + \frac{R_w\tilde{\lambda}^2}{\ell}\right)\tan\tilde{\lambda} = \tilde{\lambda}(1 - R_w\mathcal{K}). \tag{64}$$

The graphical solutions to this equation are the intersections of $\mathcal{G}(\tilde{\lambda})$ with the straight line described by the right hand side of (64). Using the same input parameters as in Section 5 the details of this solution are shown in Appendix 3.

For $R_w = 0$ Equation (64) reduces to Equation (H.20) of [13].

Equation (64) has a countable number of solutions (eigenvalues)

$$0 < \lambda_1 < \lambda_2 < ... < \lambda_n < ... \tag{65}$$

For each of these eigenvalues Solutions (59) can be presented as:

$$v_n = A_n \sin\left(\frac{\lambda_n\mathcal{R}}{R_d}\right) + B_n \cos\left(\frac{\lambda_n\mathcal{R}}{R_d}\right), \tag{66}$$

where $n = 1, 2....$

As in the case of $p < 0$ we assume that $A_n = 1$, which implies that $B_n = R_w\lambda_n/R_d$, and rewrite (66) as:

$$v_n = \sin\left(\frac{\lambda_n\mathcal{R}}{R_d}\right) + \frac{R_w\lambda_n}{R_d}\cos\left(\frac{\lambda_n\mathcal{R}}{R_d}\right). \tag{67}$$

Formula (67) can be presented in an alternative form:

$$v_n = A_{Yn}\sin\left(\frac{\lambda_n\mathcal{R}}{R_d} + \eta_{Yn}\right). \tag{68}$$

To obtain explicit expressions for coefficients A_{Yn} and η_{Yn} we rewrite (68) as

$$v_n = A_{Yn}\sin\left(\frac{\lambda_n\mathcal{R}}{R_d}\right)\cos\eta_{Yn} + A_{Yn}\cos\left(\frac{\lambda_n\mathcal{R}}{R_d}\right)\sin\eta_{Yn}. \tag{69}$$

Comparing (67) and (69) we obtain:

$$\cos\eta_{Yn} = \frac{1}{A_{Yn}}, \quad \sin\eta_{Yn} = \frac{\lambda_n R_w}{A_{Yn}R_d}, \quad \tan\eta_{Yn} = \frac{R_w\lambda_n}{R_d}. \tag{70}$$

Remembering that

$$\cos^2\eta_{Yn}+\sin^2\eta_{Yn}=\left(\frac{1}{A_{Yn}}\right)^2+\left(\frac{R_w\lambda_n}{A_{Yn}R_d}\right)^2=1$$

we obtain

$$A_{Yn}=\sqrt{1+\left(\frac{R_w\lambda_n}{R_d}\right)^2}. \tag{71}$$

For $R_w=0$ Equations (67) and (68) reduce to Equation (H.21) of [13].

Orthogonality and norms of v_n $(n=0,1,2....)$

The orthogonality of v_n for $\mathcal{R}$ in the range 0 to R_d-R_w can be proven as in [13] for the case when $R_w=0$. Also, it follows from the general theory of the Sturm-Liouville boundary value problem [26]. Completeness of these functions follows from the theory of the Sturm-Liouville boundary value problem [26] remembering that we have found all solutions to this problem.

In what follows, the norms of v_0 and v_n $(n\geq 1)$ are calculated:

$$\begin{aligned}\|v_0(\mathcal{R})\|^2&=\int_0^\ell v_0^2(\mathcal{R})\,\mathrm{d}\mathcal{R}=A_{Y0}^2\int_0^\ell\sinh^2\left(\frac{\lambda_0\mathcal{R}}{R_d}+\eta_{Y0}\right)\mathrm{d}\mathcal{R}\\&=\frac{A_{Y0}^2}{2}\left(\frac{R_d}{2\lambda_0}\sinh\Big(2\left(\frac{\lambda_0\mathcal{R}}{R_d}+\eta_{Y0}\right)\Big)-\mathcal{R}\right)\Bigg|_0^\ell\\&=\frac{1-\left(\frac{\lambda_0R_w}{R_d}\right)^2}{2}\left[\frac{R_d}{\lambda_0}\frac{\tanh\Big(\frac{\lambda_0\ell}{R_d}+\eta_{Y0}\Big)}{1-\tanh^2\Big(\frac{\lambda_0\ell}{R_d}+\eta_{Y0}\Big)}-\frac{R_d}{\lambda_0}\frac{\tanh\eta_{Y0}}{1-\tanh^2\eta_{Y0}}-\ell\right]\\&=\frac{1-\left(\frac{\lambda_0R_w}{R_d}\right)^2}{2}\left(\frac{\mathcal{K}}{\mathcal{K}^2-\left(\frac{\lambda_0}{R_d}\right)^2}-\frac{R_w}{1-\left(\frac{\lambda_0R_w}{R_d}\right)^2}-\ell\right),\end{aligned} \tag{72}$$

$$\begin{aligned}\|v_n(\mathcal{R})\|^2&=\int_0^\ell v_n^2(\mathcal{R})\,\mathrm{d}\mathcal{R}=A_{Yn}^2\int_0^\ell\sin^2\left(\frac{\lambda_n\mathcal{R}}{R_d}+\eta_{Yn}\right)\mathrm{d}\mathcal{R}\\&=\frac{A_{Yn}^2}{2}\left(\mathcal{R}-\frac{R_d}{2\lambda_n}\sin\Big(2\left(\frac{\lambda_n\mathcal{R}}{R_d}+\eta_{Yn}\right)\Big)\right)\Bigg|_0^\ell\end{aligned}$$

$$= \frac{1+\left(\frac{\lambda_n R_w}{R_d}\right)^2}{2}\left[\ell - \frac{R_d}{\lambda_n}\frac{\tan\left(\frac{\lambda_n \ell}{R_d}+\eta_{Yn}\right)}{1+\tan^2\left(\frac{\lambda_n \ell}{R_d}+\eta_{Yn}\right)} + \frac{R_d}{\lambda_n}\frac{\tan\eta_{Yn}}{1+\tan^2\eta_{Yn}}\right]$$

$$= \frac{1+\left(\frac{\lambda_n R_w}{R_d}\right)^2}{2}\left[\ell + \frac{R_w}{1+\left(\lambda_n R_w/R_d\right)^2} - \frac{\mathcal{K}}{\mathcal{K}^2+\left(\lambda_n/R_d\right)^2}\right]. \tag{73}$$

In the limit when $R_w = 0$ Equations (72) and (73) reduce to Expressions (H.17) and (H.22) of [13], respectively.

Calculation of coefficients Θ_n in Expansion (40)

Having substituted (40) into (36) we obtain:

$$\sum_{n=0}^{\infty}\Theta_n'(t)v_n(\mathcal{R}) = D_l\sum_{n=0}^{\infty}\Theta_n(t)v_n''(\mathcal{R}), \tag{74}$$

where

$$\Theta_n' = \frac{\mathrm{d}\Theta_n}{\mathrm{d}t};\quad v_n''(\mathcal{R}) = \frac{\mathrm{d}^2 v_n}{\mathrm{d}\mathcal{R}^2}.$$

Remembering that

$$\frac{\partial^2 v_0}{\partial\mathcal{R}^2} = \left(\frac{\lambda_0}{R_d}\right)^2 v_0,\quad \frac{\partial^2 v_n}{\partial\mathcal{R}^2} = -\left(\frac{\lambda_n}{R_d}\right)^2 v_n \quad (n\geq 1), \tag{75}$$

and the uniqueness of the Fourier expansion (Equation (74) is satisfied only when it is satisfied for each term), the following equations for Θ_n are obtained:

$$\Theta_0'(t) = D_l\left(\frac{\lambda_0}{R_d}\right)^2\Theta_0(t), \tag{76}$$

$$\Theta_n'(t) = -D_l\left(\frac{\lambda_n}{R_d}\right)^2\Theta_n(t),\quad n\geq 1. \tag{77}$$

To solve Equations (76) and (77) we need to find the initial conditions $\Theta_n(0)$ for $n\geq 0$. To find $\Theta_n(0)$ we substitute (40) into (39) to obtain

$$\sum_{n=0}^{\infty}\Theta_n(0)v_n(\mathcal{R}) = (\mathcal{R}+R_w)\left(Y_{li0}(\mathcal{R}+R_w)-\epsilon_0\right). \tag{78}$$

Expanding the right hand side of (78) into a Fourier series with respect to functions v_n we can rewrite the latter equation as:

$$\sum_{n=0}^{\infty} \Theta_n(0) v_n(\mathcal{R}) = \sum_{n=0}^{\infty} \left(q_{in} - \epsilon_0 Q_n\right) v_n(\mathcal{R}), \tag{79}$$

where

$$q_{in} = \frac{1}{||v_n||^2} \int_0^{\ell} (\mathcal{R} + R_w) Y_{li0}(\mathcal{R} + R_w) v_n(\mathcal{R}) \mathrm{d}\mathcal{R} \tag{80}$$

$$Q_n = \frac{1}{||v_n||^2} \int_0^{\ell} (\mathcal{R} + R_w) v_n(\mathcal{R}) \mathrm{d}\mathcal{R}. \tag{81}$$

The details of the derivation of the explicit expressions for Q_n are presented in Appendix 2.

Equation (79) is satisfied if and only if it is satisfied for each term in the Fourier series. Hence,

$$\Theta_n(0) = q_{in} - \epsilon_0 Q_n, \quad n = 0, 1, 2, ... \tag{82}$$

Remembering (82), solutions to Equations (76) and (77) can be presented as:

$$\Theta_0(t) = \exp\left[D_l \left(\frac{\lambda_0}{R_d}\right)^2 t\right] \left[q_{i0} - \epsilon_0 Q_0\right], \tag{83}$$

$$\Theta_n(t) = \exp\left[-D_l \left(\frac{\lambda_n}{R_d}\right)^2 t\right] \left[q_{in} - \epsilon_0 Q_n\right], \quad n \geq 1. \tag{84}$$

Having substituted (83) and (84) into (40), using the definitions of u and y the final solution to Equation (7), subject to boundary conditions (8)-(9) and initial condition (11), is obtained as Expression (13).

In the limit when $R_w = 0$, $\mathcal{R} = R$ and Expression (13) reduces to Expression (5.18) of [13].

Solution (13) could also be obtained from the general solution to Equation (36) subject to boundary and initial conditions (37)-(39) in the form [27]:

$$u(\mathcal{R}, t) = \int_0^{\ell} \Psi(\mathcal{R}, \xi, t) g(\xi) \, \mathrm{d}\xi, \tag{85}$$

where

$$\Psi(\mathcal{R}, \xi, t) = \sum_{n=0}^{\infty} \frac{1}{\|v_n\|^2} v_n(\mathcal{R}) v_n(\xi) \exp\left(D p_n t\right), \tag{86}$$

$$g = (\mathcal{R} + R_w)\Big(Y_{li0}(\mathcal{R} + R_w) - \epsilon_0\Big),$$

v_n are the eigenfunctions corresponding to eigenvalues p_n of the Sturm–Liouville problem (see Equation (41)) with the corresponding boundary conditions.

Appendix 2

Calculations of the expressions for Q_n based on (81)

Having substituted (51) into (81) we obtain:

$$Q_0 = \frac{1}{\|v_0\|^2}\int_0^\ell \Big[\sinh\left(\frac{\lambda_0\mathcal{R}}{R_d}\right) + \frac{\lambda_0 R_w}{R_d}\cosh\left(\frac{\lambda_0\mathcal{R}}{R_d}\right)\Big]\Big[(\mathcal{R}+R_w)\Big]\,\mathrm{d}\mathcal{R}$$

$$= \frac{-1}{\|v_0\|^2}\left\{-\frac{R_d(R_d-R_w)}{\lambda_0}\cosh\Big[\frac{\lambda_0}{R_d}(R_d-R_w)\Big] + \left(\frac{R_d^2}{\lambda_0^2} - R_wR_d\right)\sinh\Big[\frac{\lambda_0}{R_d}(R_d-R_w)\Big]\right\}. \tag{87}$$

Having substituted (67) into (81) we obtain:

$$Q_n = \frac{1}{\|v_n\|^2}\int_0^\ell \Big[\sin\left(\frac{\lambda_n\mathcal{R}}{R_d}\right) + \frac{\lambda_n R_w}{R_d}\cos\left(\frac{\lambda_n\mathcal{R}}{R_d}\right)\Big]\Big[\mathcal{R}+R_w\Big]\,\mathrm{d}\mathcal{R}$$

$$= \frac{1}{\|v_n\|^2}\left\{-\frac{R_d(R_d-R_w)}{\lambda_n}\cos\Big[\frac{\lambda_n}{R_d}(R_d-R_w)\Big] + \left(\frac{R_d^2}{\lambda_n^2} + R_wR_d\right)\sin\Big[\frac{\lambda_n}{R_d}(R_d-R_w)\Big]\right\}, \tag{88}$$

where $n \geq 1$.

In the limit $R_w = 0$, Expressions (87) and (88) reduce to Expression (H.29) of [13]. When reducing (87) and (88) to the latter expression we took into account that for $R_w = 0$:

$$\frac{\lambda_0}{R_d}\cosh\lambda_0 = \mathcal{K}\sinh\lambda_0,$$

$$\frac{\lambda_n}{R_d}\cos\lambda_n = \mathcal{K}\sin\lambda_n \quad n \geq 1.$$

These formulae follow from boundary condition (37). Note that λ used in Expression (H.29) of [13] corresponds to $\tilde{\lambda}$ used in our paper.

Appendix 3

Graphical solutions of (14) and (15)

The aim of this Appendix is to present graphical illustrations of the solutions of Equations (14) and (15) for the values of parameters typical for kerosene droplet heating and evaporation in a heating chamber at atmospheric pressure and ambient temperature 473 K. The initial droplet and water sub-droplet radii are taken equal to 0.85 mm and 0.395 mm, which corresponds to a water volume fraction equal to 10%. Thus $\ell = 0.455 \times 10^{-3}$ m. As in our analysis in Section 5 we assumed that $D_l = 1.1043 \times 10^{-9}$ m^2/s. Focusing on droplet evaporation at $t = 0$ we assumed that $\alpha = 8.2254 \times 10^{-8}$ m/s, which leads to $\mathcal{K} = 1250.9562$ 1/m.

For these values of input parameters, the plots of the left ($\mathcal{F}$) and right hand sides of (14) versus λ are shown by dotted and solid curves in Figure 4(a), respectively. Note that the right hand side of this equation is a linear function of λ. As can be seen in this figure, the curves intersect at one point; at $\lambda = 0.4617$. Plots similar to those shown in Figure 4(a), but ignoring the contribution of water ($R_w = 0$) are shown in Figure 4(b). Comparing Figures 4(a) and 4(b), it can be seen that the curves are strongly affected by the value of R_w, but the values of λ at which they intersect are rather close. They intersect at $\lambda = 0.4387$ for the case shown in Figure 4(b).

Using the same values of input parameters, the plots of the left ($\mathcal{G}$) and right hand sides of (15) versus λ are shown by dotted and solid curves in Figure 5(a), respectively. As in the case of Figure 4(a), the right hand side of (15) is a linear function of λ. As can be seen in this figure, in contrast to Figure 4(a), the curves intersect at an infinite number of points: $\lambda_1 = 6.1712$, $\lambda_2 = 11.8939$ etc. Plots similar to those shown in Figure 5(a), but ignoring the contribution of water ($R_w = 0$) are shown in Figure 5(b). In contrast to the cases shown in Figure 4, the values of λ at which they intersect are strongly affected by the presence of water. In the case shown in Figure 5(b) the curves intersect at $\lambda_1 = 4.4793$, $\lambda_2 = 7.7172$ etc.

Appendix 4

Verification of the numerical code

Analytical solution (13) in the limit when $R_w = 0$ was implemented into ANSYS Fluent via User Defined Functions (UDF) and used at each time

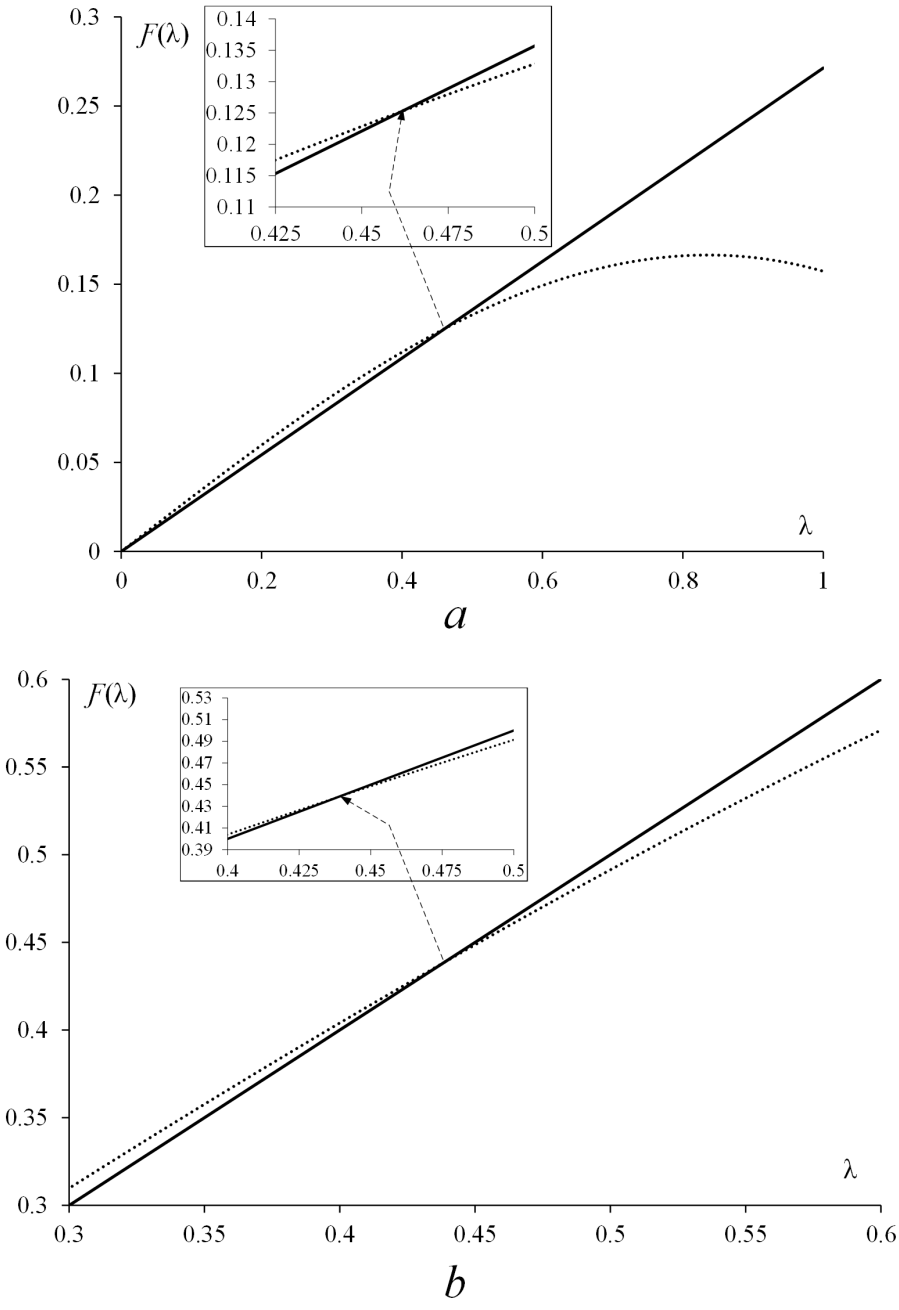

Figure 4: The plots of the left (dashed) and right (solid) hand sides of Equation (14) versus λ for typical kerosene droplets for the cases when $R_w = 0.395$ mm (a) and $R_w = 0$ (b).

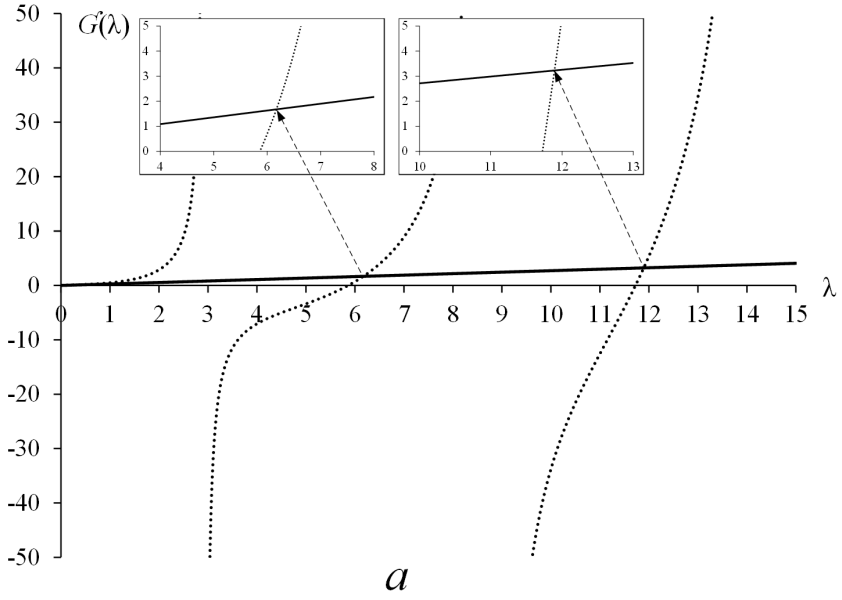

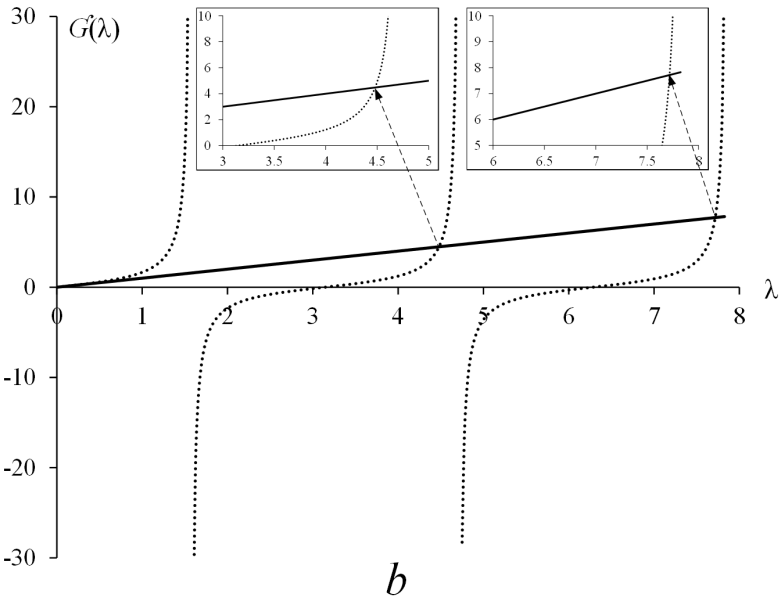

Figure 5: The same as Figure 4 but for Equation (15).

step of the calculations performed by this software [18]. In what follows, the results of these calculations are compared with those predicted by the numerical code described in Section 3 in the limit when $R_w = 0$ for heating/cooling and evaporation of acetone/ethanol mixture droplets. The focus will be on the case when the mass fractions of ethanol and acetone were 25% and 75%, respectively. The input parameters used in calculations were the same as shown in Table 1 of [18].

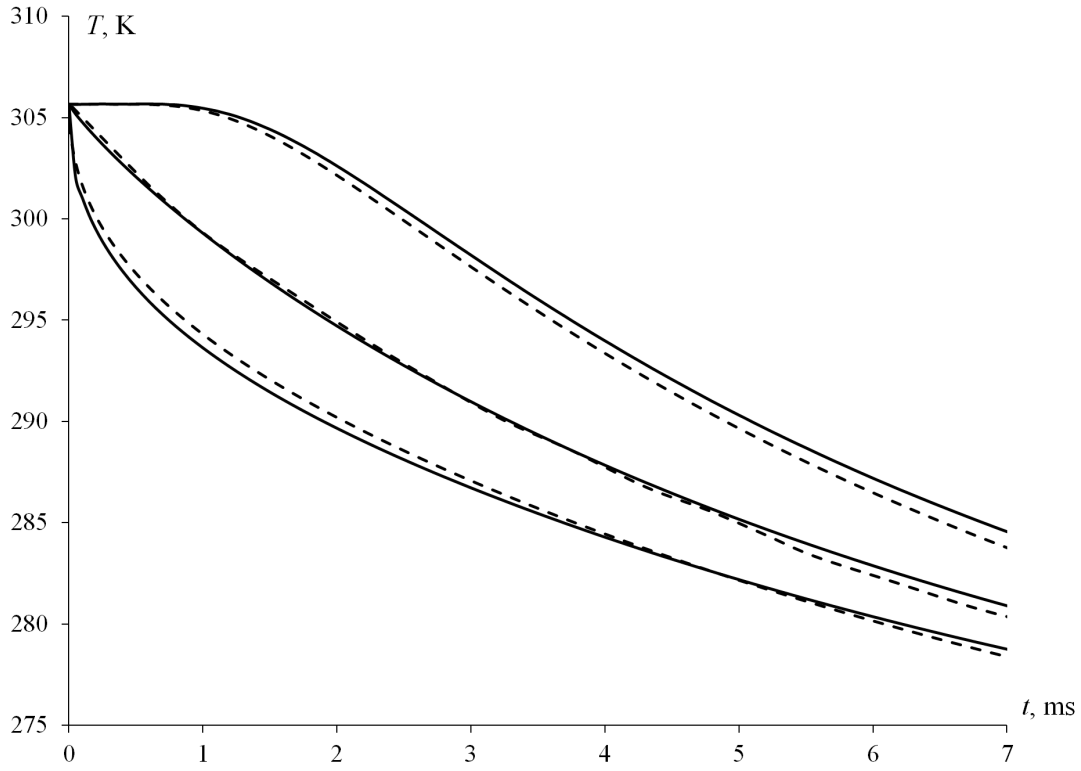

Figure 6: Time evolution of a 25% ethanol/75% acetone droplet surface (bottom curves), average (middle curves) and central (top curves) temperatures (T_s, $T_{\rm av}$ and T_c) as predicted by the customised version of ANSYS Fluent (dashed curves) and the new numerical code (solid curves). The input parameters are shown in Table 1 of [18].

The time evolution of the surface, average and central temperatures of ethanol/acetone droplets predicted by the customised version of ANSYS Fluent and the newly developed numerical code is presented in Figure 6. As follows from this figure the values of temperatures predicted by both codes

are reasonably close. The deviation between the predicted temperatures does not exceed 0.2218%. This is comparable with the deviation between the predictions of the customised version of ANSYS Fluent and the in-house code in which the analytical solution for $R_w = 0$ was originally used (0.1636%) [18]. Possible reasons for this deviation are discussed in [18].

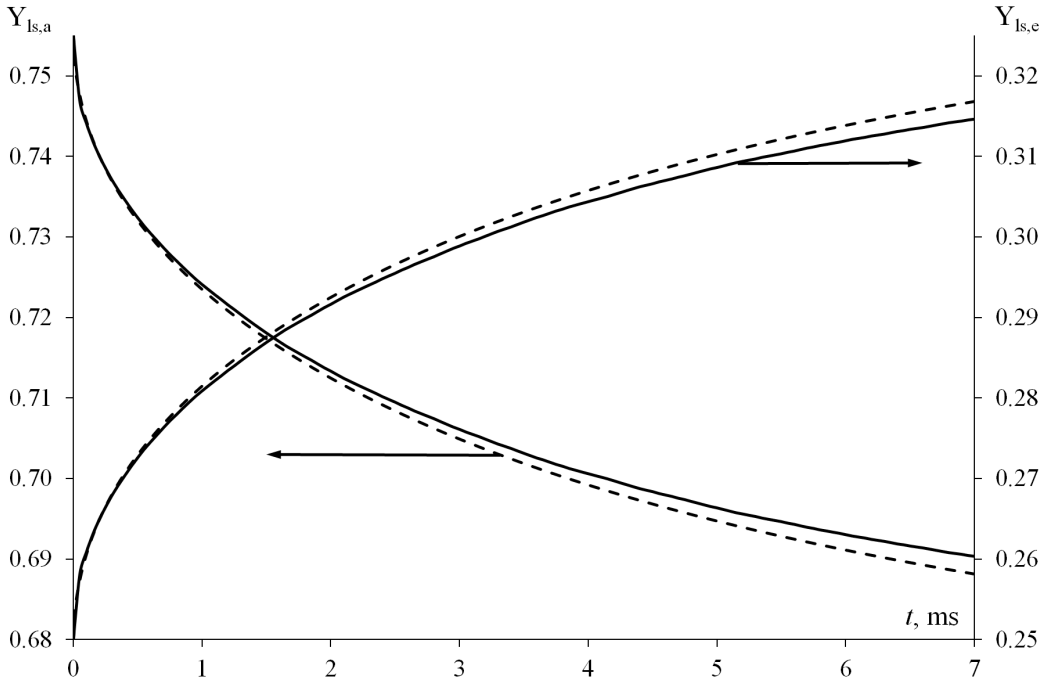

Figure 7: Time evolution of surface mass fractions of ethanol ($Y_{ls,e}$) and acetone ($Y_{ls,a}$) for the same droplet as in Figure 6, predicted by the customised version of ANSYS Fluent (dashed curves) and the new numerical code (solid curves).

The results of calculation of the time evolution of mass fractions of acetone and ethanol for the same droplets as in Figure 6 are presented in Figure 7. As follows from the latter figure, the results predicted by both codes are reasonably close although the deviation between them is larger than in the case shown in Figure 6 (0.3226%). This deviation is comparable with the deviation between the predictions of the customised version of ANSYS Fluent and the in-house code in which the analytical solution for $R_w = 0$

was originally used (0.7933%) [18]. This allows us to conclude that our new numerical code is verified in the limiting case of $R_w = 0$.

References

[1] R. Vigneswaran, D. Balasubramanian, B.D.S. Sastha Performance, emission and combustion characteristics of unmodified diesel engine with titanium dioxide (TiO_2) nano particle along with water-in-diesel emulsion fuel, Fuel 285 (2021) 119115. https://doi.org/10.1016/j.fuel.2020.119115.

[2] S.S. Sazhin, T. Bar-Kohany, Z. Nissar, D.V. Antonov, P.A. Strizhak, O. Rybdylova, A new approach to modelling micro-explosions in composite droplets, Int. J of Heat and Mass Transfer 161 (2020) 120238. https://doi.org/10.1016/j.ijheatmasstransfer.2020.120238.

[3] D.V. Antonov, P.A. Strizhak, R.M. Fedorenko, Z. Nissar, S.S. Sazhin, Puffing and microexplosions in rapeseed oil/water droplets: the effects of coal micro-particles in water, Fuel 289 (2021) 119814. https://doi.org/10.1016/j.fuel.2020.119814.

[4] S. Fostiropoulos, G. Strotos, N. Nikolopoulos, M. Gavaises, Numerical investigation of heavy fuel oil droplet breakup enhancement with water emulsions, Fuel 278 (2020) 118381. https://doi.org/10.1016/j.fuel.2020.118381.

[5] J. Shinjo, J. Xia, L.C. Ganippa, A. Megaritis, Physics of puffing and microexplosion of emulsion fuel droplets, Phys Fluids 25 (2014) 103302. https://doi.org/10.1063/1.4897918.

[6] J. Shinjo, J. Xia, A. Megaritis, L.C. Ganippa, R.F. Cracknell, Modeling temperature distribution inside a emulsion fuel droplet under convective heating: A key to predicting microexplosion and puffing, Atomization and Sprays 26 (2016) 551-583. https://doi.org/10.1615/ATOMIZSPR.2015013302.

[7] J. Shinjo, J. Xia, Combustion characteristics of a single decane/ethanol emulsion droplet and a droplet group under puffing conditions, Proceedings of the Combustion Institute 36 (2017) 2513-2521. http://dx.doi.org/10.1016/j.proci.2016.06.191.

[8] O.G. Girin, Dynamics of the emulsified fuel droplet micro-explosion, Atomization and Sprays 27 (2017) 407-422. http://dx.doi.org/10.1615/AtomizSpr.2017017143.

[9] S. Shen, Z. Che, T. Wang, Z. Yue, K. Sun, S. Som, A model for droplet heating and evaporation of water-in-oil emulsified fuel, Fuel 266 (2020) 116710. https://doi.org/10.1016/j.fuel.2019.116710.

[10] P. Yi, T. Li, Y. Fu, S. Xie, Transcritical evaporation and micro-explosion of ethanol-diesel droplets under diesel engine-like conditions, Fuel 284 (2021) 118892. https://doi.org/10.1016/j.fuel.2020.118892.

[11] S. Fostiropoulos, G. Strotos, N. Nikolopoulos, M. Gavaises, A simple model for breakup time prediction of water-heavy fuel oil emulsion droplets. Int. J Heat and Mass Transfer 164 (2021) 120581. https://doi.org/10.1016/j.ijheatmasstransfer.2020.120581.

[12] S.S. Sazhin, M. Al Qubeissi, R. Nasiri, V.M. Gun'ko, A.E. Elwardany, F. Lemoine, F. Grisch, M.R. Heikal, A multi-dimensional quasi-discrete model for the analysis of Diesel fuel droplet heating and evaporation, Fuel 129 (2014) 238-266. https://doi.org/10.1016/j.fuel.2014.03.028.

[13] S.S. Sazhin, Droplets and Sprays, Springer 2014.

[14] B. Abramzon, W.A. Sirignano, Droplet vaporization model for spray combustion calculations, Int. J. Heat Mass Transfer 32 (1989) 1605-1618. https://doi.org/10.1016/0017-9310(89)90043-4.

[15] P.A. Strizhak, R.S. Volkov, G. Castanet, F. Lemoine, O. Rybdylova, S.S. Sazhin, Heating and evaporation of suspended water droplets: experimental studies and modelling, Int. J. Heat and Mass Transfer 127 (2018) 92-106. https://doi.org/10.1016/j.ijheatmasstransfer.2018.06.103.

[16] S. Tonini, G.E. Cossali, A novel formulation of multi-component drop evaporation models for spray applications, Int. J. Thermal Science 89 (2015) 245-253. https://doi.org/10.1016/j.ijthermalsci.2014.10.016.

[17] S. Tonini, G.E. Cossali, A multi-component drop evaporation model based on analytical solution of Stefan-Maxwell equations. Int. J Heat Mass Transfer 92 (2016) 184-189. https://doi.org/10.1016/j.ijheatmasstransfer.2015.08.014.

[18] O. Rybdylova, L. Poulton, M. Al Qubeissi, A.E. Elwardany, C. Crua, T. Khan, S.S. Sazhin, A model for multi-component droplet heating and evaporation and its implementation into ANSYS Fluent, Int. Commun Heat Mass Transfer 90 (2018) 29-33. https://doi.org/10.1016/j.icheatmasstransfer.2017.10.018.

[19] D.V. Antonov, M.V. Piskunov, P.A. Strizhak, Breakup and explosion of droplets of two immiscible fluids and emulsions, Int. J. Thermal Science 142 (2019) 30-41. https://doi.org/10.1016/j.ijthermalsci.2019.04.011.

[20] D.V. Antonov, G.V. Kuznetsov, P.A. Strizhak, O. Rybdylova, S.S. Sazhin, Micro-explosion and autoignition of composite fuel/water droplets, Combust. Flame 210 (2019) 479-489. https://doi.org/10.1016/j.combustflame.2019.09.004.

[21] D.V. Antonov, G.V. Kuznetsov, P.A. Strizhak, Comparison of the characteristics of micro-explosion and ignition of two-fluid water-based droplets, emulsions and suspensions, moving in the high-temperature oxidizer medium, Acta Astronaut. 160 (2019) 258-269. https://doi.org/10.1016/j.actaastro.2019.04.048.

[22] D.V. Antonov, G.S. Nyashina, P.A. Strizhak, D.S. Romanov, Micro-explosive droplet fragmentation of environmentally promising coal-water slurries containing petrochemicals, Fuel 283 (2021) 118949. https://doi.org/10.1016/j.fuel.2020.118949.

[23] L. Poulton, O. Rybdylova, I.A. Zubrilin, S.G. Matveev, N.I. Gurakov, M. Al Qubeissi, N. Al-Esawi, T. Khan, V.M. Gun'ko, S.S. Sazhin, Modelling of multi-component kerosene and surrogate fuel droplet heating and evaporation characteristics: A comparative analysis, Fuel 269 (2020) 117115. https://doi.org/10.1016/j.fuel.2020.117115.

[24] A.P. Pinheiro, O. Rybdylova, I.A. Zubrilin, S.S. Sazhin, F.L.S. Filho, J.M. Vedovotto, Modelling of aviation kerosene droplet heating and evaporation using complete fuel composition and surrogates, Fuel 305 (2021) 121564. https://doi.org/10.1016/j.fuel.2021.121564.

[25] S.S. Sazhin, M. Al Qubeissi, R. Kolodnytska, A.E. Elwardany, R. Nasiri, M.R. Heikal, Modelling of biodiesel fuel droplet heating and evaporation, Fuel 115 (2014) 559-572. https://doi.org/10.1016/j.fuel.2013.07.031.

[26] W. E. Boyce, R C. Di Prima, Elementary Differential Equations and Boundary Value Problems. 11th Edition. Wiley and Sons Inc., 2017

[27] A. Polyanin, Handbook of Linear Partial Differential Equations for Engineers and Scientists, Chapman & Hall/CRC Press, Boca Raton, 2002.